


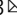




Kramers Weyl semimetals as quantum solenoids and their applications in spin-orbit torque devices

Wen-Yu He¹, Xiao Yan Xu² & K. T. Law³

Kramers Weyl semimetals are Weyl semimetals that have Weyl points pinned at the time reversal invariant momenta. Recently it has been discovered that all chiral crystals host Weyl points at time reversal invariant momenta, so metals with chiral lattice symmetry all belong to the category of Kramers Weyl semimetals. In this work, we show that due to the chiral lattice symmetry, Kramers Weyl semimetals have the unique longitudinal magnetoelectric effect in which the charge current induced spin and orbital magnetization is parallel to the direction of the current. This feature allows Kramers Weyl semimetals to act as nanoscale quantum solenoids with both orbital and spin magnetization. As the moving electrons of Kramers Weyl semimetal can generate longitudinal magnetization, Kramers Weyl semimetals can be used for new designs of spin-orbit torque devices with all electric control of magnetization switching for magnets with perpendicular magnetic anisotropy.

¹Department of Physics, Massachusetts Institute of Technology, Cambridge, MA 02139, USA. ²Department of Physics, University of California at San Diego, La Jolla, CA 92093, USA. ³Department of Physics, Hong Kong University of Science and Technology, Clear Water Bay, Hong Kong, China.
email: wenyuhe@mit.edu; phlaw@ust.hk

Weyl semimetals are nodal topological materials characterised by isolated band touching points, called Weyl points, in 3D momentum space^{1–4}. Due to the Weyl points, which act as the monopoles of the Berry curvature in the momentum space^{1–4}, Weyl semimetals exhibit many exotic properties such as the chiral magnetic effect^{5–8}, the presence of topologically protected Fermi arcs states^{1–4,9,10}, unconventional quantum oscillations¹¹, and novel optical phenomenon^{12–14}. Recently, a new type of Weyl semimetals called Kramers Weyl semimetals (KWS) in chiral crystals have been discovered^{15–24}. Chiral crystals are crystals which lack inversion, mirror and improper rotation symmetries. As a result, a chiral crystal has a definite handedness and can be described by the 11 chiral point groups. It was shown that generally, due to the low lattice symmetry, band splittings appear away from time-reversal invariant points in momentum space and result in Kramers Weyl points pinned at time-reversal invariant momenta. However, it is not clear how the properties of KWS are distinct from that of other Weyl semimetals with non-chiral point group symmetry.

In this work, we point out that the chiral lattice symmetry in KWS brings about a unique property: an electric field applied along the principal symmetry axis of the crystal would induce spin and orbital magnetization which is parallel to the applied electric field. This is in sharp contrast to the case of all other noncentrosymmetric Weyl semimetals which give zero magnetoelectric response if the electric field is applied along the principal symmetry axis. This distinctive longitudinal magnetoelectric response involves both the spin²⁵ and orbital magnetization^{26,27}, and it arises from the special form of the spin-orbit coupling (SOC) of KWS. Importantly, for the representative KWS $K_2Sn_2O_3$ and $RhSn$ in the T point group we considered, the induced magnetization at a given electric field can be two to three orders of magnitude larger than the magnetization induced in materials with the strong Rashba spin-orbit couplings such as in Au (111) surfaces and Bi/Ag bilayers^{28,29}. Therefore, if the electrons which carry both orbital and spin angular momentum in the KWS are injected into a ferromagnetic layer, the torque induced by the electrons can cause magnetization switching in the ferromagnetic layer. As a result, we propose a KWS based magnetization switching device that is different from the magnetic tunneling device based on spin transfer torque^{30,31} and the conventional spin orbit torque devices^{30–33}. The new KWS based devices allow all electric control of magnetic switching for ferromagnets with perpendicular magnetic anisotropy, which is important for high density magnetic memories.

Results

Effective Hamiltonians for Kramers Weyl semimetals. In chiral crystals which respect time reversal symmetry, the energy bands are at least doubly degenerate at time-reversal invariant momenta due to the Kramers theorem. In the absence of inversion, mirror and improper rotation symmetries in chiral crystals, and away from the time-reversal invariant points, SOC would lift the Kramers degeneracy in momentum space to create Kramers Weyl points¹⁸. To be more specific, in the spin $\frac{1}{2}$ basis $\psi_{\mathbf{k}} = [\phi_{\mathbf{k},\uparrow}, \phi_{\mathbf{k},\downarrow}]^T$, which satisfies the relation $\Theta\psi_{\mathbf{k}} = i\sigma_y\psi_{-\mathbf{k}}$ under time-reversal operation $\Theta = i\sigma_yK$, the effective Hamiltonian $H_0(\mathbf{k})$ can be obtained through standard $\mathbf{k} \cdot \mathbf{p}$ method¹⁸. Up to second order near a time-reversal invariant momentum \mathbf{k}_0 , the general form of the Kramers Weyl Hamiltonian can be written as

$$H_0(\mathbf{k}) = \sum_{i,j} \frac{\hbar^2}{2m_{ij}} k_i k_j + \sigma_i \hbar v_{ij} k_j. \quad (1)$$

Here, \mathbf{k} is measured from \mathbf{k}_0 , $i, j = x, y, z$, m_{ij} is the effective mass tensor, σ_i are the Pauli matrices in spin space, and v_{ij} is the SOC

pseudotensor. In chiral crystals, the little group at \mathbf{k}_0 is isomorphic to a chiral point group which guarantees $\det(v) \neq 0$ so that the Kramers Weyl point emerges at $\mathbf{k} = 0$.

In the KWS, the specific forms of the SOC that creates the Weyl point are determined by the point group symmetry as $v = \det(\hat{R})\hat{R}v\hat{R}^T$, with \hat{R} the symmetry transformation matrix. In materials within the cubic point group $\{T, O\}$ such as $K_2Sn_2O_3$ ¹⁸, $RhSi$ ¹⁹, $CoSi$ ^{19–21}, $AlPt$ ²², $PtGa$ ²³, and $PdGa$ ²⁴ of cubic chiral B20 structure³⁴, at \mathbf{k}_0 (such as the Γ point) the little group isomorphic to $\{T, O\}$ can give rise to the isotropic Weyl Hamiltonian

$$H_0(\mathbf{k}) = \frac{\hbar^2}{2m} k^2 + \hbar v \mathbf{k} \cdot \boldsymbol{\sigma}, \quad (2)$$

where the high symmetry cubic point group $\{T, O\}$ forces v_{ij} to be proportional to the identity matrix. In those materials within the point group $\{T, O\}$, the high symmetry may also enable extra multi-fold point degeneracies to appear at \mathbf{k}_0 ^{15–17}. In the materials $CsCuBr_3$ ¹⁸, elemental Te , Se ^{35–38}, etc., the dihedral point group there has lower crystal symmetry and allows the anisotropy to show up in the Weyl Hamiltonian

$$H_0(\mathbf{k}) = \sum_{i=x,y,z} \frac{\hbar^2}{2m_i} k_i^2 + \hbar v_i \sigma_i k_i. \quad (3)$$

In the materials belonging to the cyclic point group, as the crystal symmetry is further reduced, the constraints on the SOC is further reduced. The complete forms of the SOC pseudotensor v_{ij} in the KWS Hamiltonian are summarised in the Supplementary Table 1 for all the chiral point groups.

The SOC in the KWS creates the Kramers Weyl points at the time reversal invariant momenta and allows the coupling between the spin and momentum. Under an electric field, the SOC enables the charge carriers to have net magnetization and such magnetoelectric response respects the same crystal symmetry present in the SOC. As shown below, for materials with cubic point groups $\{T, O\}$, the simple form of the isotropic Weyl Hamiltonian in Eq. (2) allows us to calculate the magnetoelectric susceptibility analytically. For the KWS in dihedral and cyclic point group, the magnetoelectric responses are calculated numerically for the selected materials in Supplementary Note 1 and Supplementary Note 2 respectively.

Magnetoelectric pseudotensors and their symmetry properties.

In magnetoelectric effects, induced magnetization \mathbf{M} and the applied electric field \mathbf{E} are related by the magnetoelectric pseudotensor α such that:

$$\mathbf{M}_i = \sum_{j=x,y,z} \alpha_{ij} E_j, \quad (4)$$

where $i, j = x, y, z$ and α_{ij} are elements of the magnetoelectric pseudotensor α . For a generic Hamiltonian

$$\mathcal{H} = \sum_{\nu,\nu',\mathbf{k}} c_{\nu,\mathbf{k}}^\dagger H_{0,\nu\nu'}(\mathbf{k}) c_{\nu',\mathbf{k}}, \quad (5)$$

where $c_{\nu,\mathbf{k}}^\dagger$ ($c_{\nu,\mathbf{k}}$) is the creation (annihilation) operator, $H_{0,\nu\nu'}(\mathbf{k})$ is the element of the Hamiltonian matrix $H_0(\mathbf{k})$, α_{ij} can be obtained from the linear response theory as^{26,27}

$$\alpha_{ij} = -\tau \frac{e}{\hbar} \frac{1}{(2\pi)^d} \int_{\text{BZ}} d\mathbf{k} \sum_n M_{n\mathbf{k},i} \nu_{n\mathbf{k},j} \frac{df(E_{n\mathbf{k}})}{dE_{n\mathbf{k}}}. \quad (6)$$

In Eq. (6), $f(E_{n\mathbf{k}})$ is the Fermi Dirac distribution function, $E_{n\mathbf{k}}$ is the energy dispersion of band n from the Hamiltonian $H_0(\mathbf{k})$, $\nu_{n\mathbf{k},j} = \frac{\partial E_{n\mathbf{k}}}{\partial k_j}$, d is the dimension of the system, τ is the effective scattering time and $i, j = x, y, z$ denote the spatial components. The total magnetic moment $\mathbf{M}_{n\mathbf{k}} = \mathbf{S}_{n\mathbf{k}} + \mathbf{m}_{n\mathbf{k}}$ carried by the

Table 1 of Magnetoelectric susceptibility pseudotensor α for the chiral crystals in the 11 chiral point groups.

Point group	α	Point group	α
O	$\begin{pmatrix} \alpha_0 & 0 & 0 \\ 0 & \alpha_0 & 0 \\ 0 & 0 & \alpha_0 \end{pmatrix}$	T	$\begin{pmatrix} \alpha_0 & 0 & 0 \\ 0 & \alpha_0 & 0 \\ 0 & 0 & \alpha_0 \end{pmatrix}$
D ₂	$\begin{pmatrix} \alpha_{xx} & 0 & 0 \\ 0 & \alpha_{yy} & 0 \\ 0 & 0 & \alpha_{zz} \end{pmatrix}$	D ₃	$\begin{pmatrix} \alpha_{\parallel} & 0 & 0 \\ 0 & \alpha_{\parallel} & 0 \\ 0 & 0 & \alpha_{zz} \end{pmatrix}$
D ₄	$\begin{pmatrix} \alpha_{\parallel} & 0 & 0 \\ 0 & \alpha_{\parallel} & 0 \\ 0 & 0 & \alpha_{zz} \end{pmatrix}$	D ₆	$\begin{pmatrix} \alpha_{\parallel} & 0 & 0 \\ 0 & \alpha_{\parallel} & 0 \\ 0 & 0 & \alpha_{zz} \end{pmatrix}$
C ₁	$\begin{pmatrix} \alpha_{xx} & \alpha_{xy} & \alpha_{xz} \\ \alpha_{yx} & \alpha_{yy} & \alpha_{yz} \\ \alpha_{zx} & \alpha_{zy} & \alpha_{zz} \end{pmatrix}$	C ₂	$\begin{pmatrix} \alpha_{xx} & \alpha_{xy} & 0 \\ \alpha_{yx} & \alpha_{yy} & 0 \\ 0 & 0 & \alpha_{zz} \end{pmatrix}$
C ₃	$\begin{pmatrix} \alpha_{\parallel} & -\alpha^- & 0 \\ \alpha^- & \alpha_{\parallel} & 0 \\ 0 & 0 & \alpha_{zz} \end{pmatrix}$	C ₄	$\begin{pmatrix} \alpha_{\parallel} & -\alpha^- & 0 \\ \alpha^- & \alpha_{\parallel} & 0 \\ 0 & 0 & \alpha_{zz} \end{pmatrix}$
C ₆	$\begin{pmatrix} \alpha_{\parallel} & -\alpha^- & 0 \\ \alpha^- & \alpha_{\parallel} & 0 \\ 0 & 0 & \alpha_{zz} \end{pmatrix}$		

α_{ij} with $i, j = x, y, z$ are in general the elements in α . In point group with symmetry, the 9 elements in α_{ij} is no longer independent. α_0 means $\alpha_0 = \alpha_{xx} = \alpha_{yy} = \alpha_{zz}$ in T and O point group. In the {C₃, C₄, C₆, D₃, D₄, D₆} group $\alpha_{xx} = \alpha_{yy}$ is then denoted as $\alpha_{\parallel} = \alpha_{xx} = \alpha_{yy}$. α^- means the antisymmetric elements as $\alpha^- = -\alpha_{yx} = \alpha_{xy}$ in group {C₃, C₄, C₆}. The principal axis of the crystal is set along z.

Bloch electrons consists of both the spin magnetic moment $S_{nk} = \langle \phi_{k,n} | \frac{1}{2} g \mu_B \boldsymbol{\sigma} | \phi_{k,n} \rangle$ and the orbital magnetic moment $m_{nk} = \frac{ie}{2\hbar} \langle \partial_k \phi_{k,n} | \times [H_0(\mathbf{k}) - E_{nk}] | \partial_k \phi_{k,n} \rangle$. Here, $\mu_B = \frac{e\hbar}{2m_e}$ is the Bohr magneton, g is the Lande g factor which is set to be 2 in our calculations and $|\phi_{k,n}\rangle$ denotes a Bloch state. As we will show explicitly below, the orbital magnetization is related to the Berry curvature of the Bloch states which has the form $\Omega_{nk} = i \langle \partial_k \phi_{k,n} | \times | \partial_k \phi_{k,n} \rangle$ ³⁹.

The linear response theory applies to generic Hamiltonians. However, to shed light on the general properties of KWS, we note that the form of α can be determined by point group symmetries which is independent of the details of the Hamiltonian. The group theory analysis of α is elaborated in the Method Section as well as in Ref.⁴⁰, and the general form for the chiral point groups is provided in Table 1. From the group theory point of view, KWS can be classified into three sub-classes. For KWS belonging to the cubic point groups {T, O}, α is proportional to the identity matrix as shown in Table 1. This implies that the induced magnetization is always parallel to the direction of the applied electric field. Therefore, these KWS can behave as classical solenoids in all electric field directions without the need to fabricate any spiral structures.

For KWS with point groups D_{*n*}, a pure longitudinal magnetization parallel to the electric field is also obtained when the electric field is applied along the direction of any of the symmetry axes. For KWS with cyclic point groups, in general, magnetization with both components parallel and perpendicular to the direction of the applied electric field are generated. Interestingly, for all other Weyl semimetals without chiral point group symmetry, the magnetoelectric response is zero if the electric field is applied along the principal axis, which can be obtained from the Supplementary Table 1. Therefore, the longitudinal magnetoelectric response along the principal symmetry axis is a very distinctive feature of KWS due to the special spin texture of KWS which determines the spin and orbital magnetization.

Combined with the effective Hamiltonian for isotropic KWS in Eq. (2), the magnetoelectric susceptibility in Eq. (6) can be

explicitly calculated and it shows how the SOC strength and band dispersion will influence the magnetoelectric response.

Longitudinal magnetoelectric response in KWS. We first consider an effective Hamiltonian which describes a Kramers Weyl point near the Γ point in chiral crystals with point groups {T, O}, where the isotropic Weyl Hamiltonian is $H_0(\mathbf{k}) = \frac{\hbar^2}{2m} \mathbf{k}^2 + \hbar v \mathbf{k} \cdot \boldsymbol{\sigma}$. At the Fermi energy $E_F = \frac{\hbar^2}{2m} k_F^2 \pm \hbar v |\mathbf{k}_F|$, there are two spherical Fermi surfaces with corresponding wave vectors $\mathbf{k}_{F\pm} = k_{F\pm} \hat{\mathbf{k}}$, where $k_{F\pm} = \frac{1}{\hbar} \sqrt{2mE_F + m^2 v^2} \mp \frac{m v}{\hbar}$ and $\hat{\mathbf{k}} = \frac{\mathbf{k}}{|\mathbf{k}|}$. The spin and orbital magnetic moments of the two Fermi surfaces with Fermi momenta $\mathbf{k}_{F\pm}$ can be written as

$$\mathbf{S}_{\mathbf{k}_{F\pm}} = \pm \frac{g}{2} \frac{e\hbar}{2m_e} \hat{\mathbf{k}}_{F\pm}, \quad \text{and} \quad \mathbf{m}_{\mathbf{k}_{F\pm}} = \frac{ev}{2} \frac{\hat{\mathbf{k}}_{F\pm}}{|\mathbf{k}_{F\pm}|}. \quad (7)$$

It is important to note that the orbital magnetic moment $\mathbf{m}_{\mathbf{k}_{F\pm}}$ is proportional to the Berry curvature generated by the Weyl point inside Fermi surfaces which is $\Omega_{\mathbf{k}_{F\pm}} = \mp \frac{\hat{\mathbf{k}}_{F\pm}}{2k_{F\pm}^2}$. The spin texture on a Fermi surface is schematically shown in Fig. 1a. It is clear that without breaking time-reversal symmetry, the total magnetic moment of all the electrons is zero. By applying an electric field, the steady state distribution of the electronic state can generate a net magnetization as indicated in Eq. (6). With this special form of spin texture of an isotropic KWS, at the Fermi energy E_F , we obtain the isotropic longitudinal magnetoelectric susceptibility α_0 as (see the method section for detailed derivation)

$$\alpha_0 = -\frac{e^2 v \tau}{6\hbar^2 \pi^2} \sqrt{2mE_F + m^2 v^2} \left(g \frac{m}{m_e} - 1 \right). \quad (8)$$

In α_0 , the first and second terms are the spin and the orbital contributions respectively. It is important to note that, for hole bands with negative effective mass, the spin and orbital contribution will always add together to enhance the magnetoelectric response. From Table 1, the magnetoelectric response of an isotropic KWS can be written as $M = \alpha_0 E$ which indicates that the magnetization induced is parallel to the applied electric field as is schematically shown in Fig. 1b. From Eq. (8), it is clear that strong Weyl SOC v , long scattering time τ and large effective mass m can give large magnetoelectric response.

To acquire a strong magnetoelectric response, it is also preferable to have long scattering time as shown in Eq. (8). In KWS, since the Kramers Weyl points are pinned at the time reversal invariant momenta, the electrons on opposite sides of the Weyl point have opposite spin. As a result, for elastic back scattering from scalar impurities, the intra Weyl pocket scattering is suppressed by the SOC, similar to the case in the surface states of topological insulators^{41–43}. For an ideal KWS that only has Fermi surfaces enclosing the Weyl point at time reversal invariant momenta, the Weyl SOC can enhance the scattering time by a factor of 3 as shown in the method section using Born approximation. Therefore, we choose a scattering time $\tau = 1$ ps, which is in the range of the inter Weyl point scattering time in TaAs^{29,44,45}. With the effective mass $m = 1.4m_e$, Weyl SOC strength $\hbar v = -70$ meV · nm, the KWS have the band dispersion shown in Fig. 1c. The isotropic magnetoelectric susceptibility α_0 as a function of Fermi energy E_F is then evaluated as shown in Fig. 1d. For the Fermi pockets enclosing a single Kramers Weyl point, the isotropic magnetoelectric susceptibility α_0 increases with the square root of the Fermi energy E_F .

To seek a large magnetoelectric response from realistic materials, we study two representative materials in the T point group: the K₂Sn₂O₃¹⁸, the RhSn³⁴. The K₂Sn₂O₃ is a small gap insulator with a Kramers Weyl point at H near the conduction

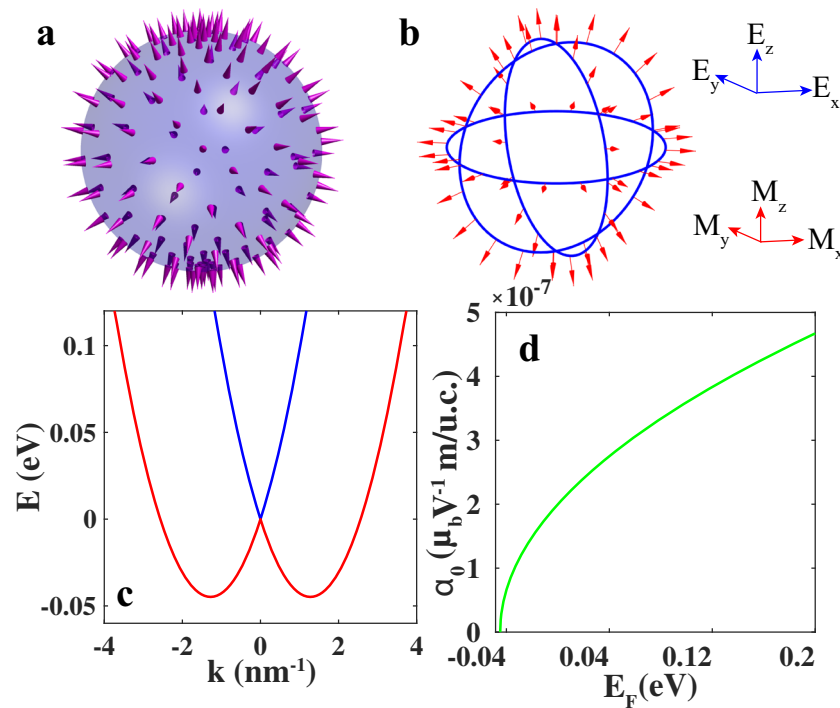


Fig. 1 The longitudinal magnetoelectric response of isotropic Kramers Weyl semimetals. **a** The Weyl spin texture of isotropic Weyl spin-orbit coupling $\hbar\mathbf{v}\mathbf{k} \cdot \boldsymbol{\sigma}$ at the Fermi surface from the band branch+. **b** The electrically induced magnetization is parallel to the applied electric field. Here blue and red coordinates are the Cartesian coordinates for the applied electric field $\mathbf{E} = (E_x, E_y, E_z)$ and the generated magnetization $\mathbf{M} = (M_x, M_y, M_z)$. **c** The energy dispersion for the isotropic chiral Weyl semimetal. The blue and red line corresponds to the + and – band branch respectively. **d** The magnetoelectric susceptibility α_0 strength as a function of the Fermi energy E_F . In the presence of external electric field, α_0 gives the number of Bohr magneton (μ_B) per unit cell (u.c.) to denote the magnetization in the material.

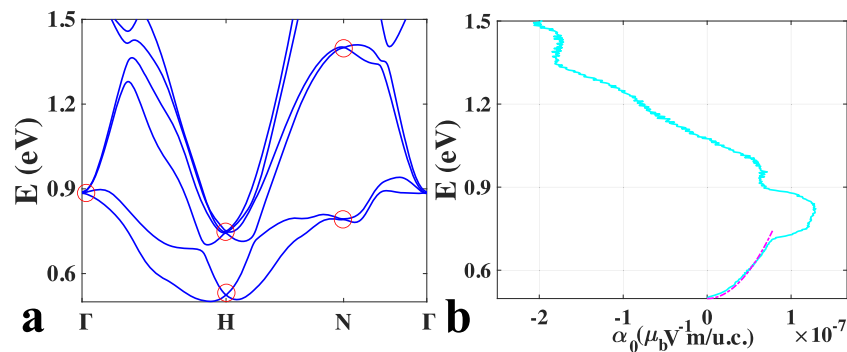


Fig. 2 The isotropic longitudinal magnetoelectric response in $\text{K}_2\text{Sn}_2\text{O}_3$. **a** The band structure of $\text{K}_2\text{Sn}_2\text{O}_3$. The red circles highlight the Kramers Weyl point as well as a multi-fold fermion in this material. **b** The isotropic longitudinal magnetoelectric susceptibility α_0 as a function of conduction band energy. Below $E = 0.7\text{eV}$, the magnetoelectric response can be well described by the analytical result from Eq. (8) with $m = 1.4 m_e$, $\hbar v = -70 \text{ meV} \cdot \text{nm}$, $\tau = 6\text{ps}$. The sudden increase of the magnetoelectric response near $E = 0.7\text{eV}$ is due to the emergence of the bands associated with the multi-fold fermion at H point of the Brillouin zone. The magenta dashed line denotes the analytical derived α_0 in Eq. (8) while the numerically obtained α_0 is plotted in a cyan solid line.

band bottom. Around the Kramers Weyl point, the conduction bands of $\text{K}_2\text{Sn}_2\text{O}_3$ have large spin splitting shown in Fig. 2a. In the slight n-doped state, the electrons will occupy the Fermi pockets enclosing the single Kramers Weyl point at H so that the isotropic Weyl Hamiltonian can be effectively described by Eq. (2), with the effective mass $m = 1.4 m_e$ and SOC strength $\hbar v = -70 \text{ meV} \cdot \text{nm}$. To validate the calculations using an effective Hamiltonian in the form of Eq. (2), a realistic tight-binding model for $\text{K}_2\text{Sn}_2\text{O}_3$ is further constructed (see the method section) to calculate the magnetoelectric susceptibility α_0 , as is shown in Fig. 2b. Below $E = 0.7\text{eV}$, only the Weyl bands enclosing the Kramers Weyl point at H are involved so that the

numerically calculated magnetoelectric susceptibility matches well with the analytical formula in Eq. (8). It is interesting to note that there is a four-fold fermion around the energy $E = 0.75 \text{ eV}$. As the Fermi surfaces enclosing multi-fold fermion also contribute to the magnetoelectric susceptibility α_0 ⁴⁶, the fourfold fermion at H point induce a sudden increase of α_0 when the chemical potential is above 0.7eV . Assuming that the chemical potential lies at $E = 0.6\text{eV}$ (about 80 meV above the Weyl point), an electric field of 10^5 V/m is enough to generate a magnetization of $0.005\mu_B$ per unit cell.

On the other hand, RhSn, which has the same B20 structure as the recently studied KWS RhSi¹⁹, is semimetallic. The SOC

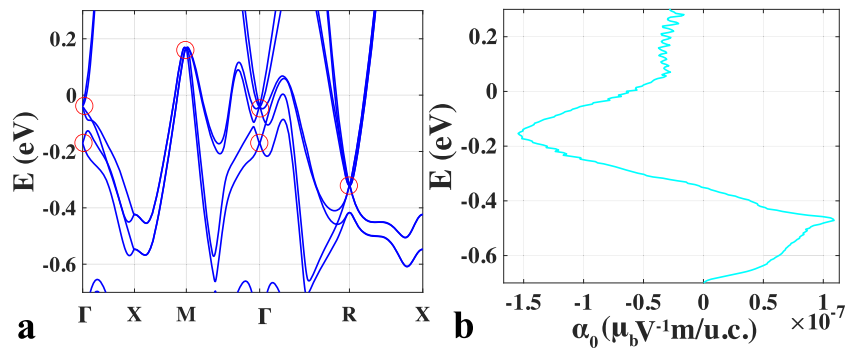


Fig. 3 The isotropic longitudinal magnetoelectric response in RhSn. **a** The band structure for RhSn. Both Kramers Weyl points as well as other multi-fold fermion band crossing points can be found. The red circles highlight the Kramers Weyl point as well as a four-fold fermion in the material. **b** The isotropic longitudinal magnetoelectric susceptibility α_0 in units of $\mu_0 V^{-1} m$ per unit cell is calculated. The effective scattering time is taken to be $\tau = 6$ ps.

generates the Kramers Weyl points at Γ as well as other multi-fold fermion band crossing points^{15–17} at the time reversal invariant momenta as shown in Fig. 3a. A fourfold fermion band crossing point near the Fermi energy is highlighted by a red circle in Fig. 3a. With the realistic tight binding model constructed from Wannier functions (see the “method” section), the magnetoelectric susceptibility α_0 is calculated in the energy range including all the bands. The results are shown in Fig. 3b. At the Fermi energy, which is near the multi-fold fermion Weyl point, an electric field of 10^5 V/m can generate a magnetization of $0.007\mu_B$ per unit cell. Compared with the magnetoelectric response of Au(111) surface and Bi/Ag bilayers which have large Rashba SOC^{28,29}, the $K_2Sn_2O_3$ and RhSn can generate magnetizations which are two to three orders of magnitude larger.

For KWS with dihedral (D_n) point groups, such as $CsCuBr_3$ ¹⁸, and elemental Te, Se^{35–38}, a pure longitudinal magnetoelectric response can also be obtained when the electric field is applied along the direction of the symmetry axes. On the other hand, for KWS with cyclic (C_n) point groups, such as $Ca_2B_5Os_3$, a longitudinal magnetoelectric response is generally accompanied with a transverse response. The calculations of magnetoelectric tensors for $CsCuBr_3$ with D_2 point group and $Ca_2B_5Os_3$ with C_2 point group can be found in the Supplementary Note 1 and Supplementary Note 2 respectively.

Discussion

We note that the current induced magnetization in Weyl semimetals was first studied by Johansson et al. in TaAs which belong to the point group C_{4v} with mirror planes²⁹. Therefore, the Weyl points appear at general \mathbf{k} points and the resulting spin polarization induced by an electric field is perpendicular to the direction of the electric field. This transverse magnetoelectric effect is similar to the case with Rashba SOC²⁵ which is a property of the polar point group as shown in Supplementary Table 1. If the applied electric field is along the principal axis, however, the magnetoelectric response is zero in TaAs as determined by the C_{4v} point group symmetry.

On the other hand, the longitudinal magnetoelectric response in Weyl semimetals was first studied by Yoda et al.^{47,48}. However, in their models, helical hopping textures^{47,48} are needed for electrons to hop in a spiral manner, imitating the movement of electrons in a classical solenoid. As a result, an orbital magnetization parallel to the direction of an applied electric field would be generated and the longitudinal magnetization is present even without spin-orbit coupling. Unfortunately, no realistic materials that possess such helical hopping textures are identified.

In this work, the finite longitudinal magnetoelectric response comes from the current induced net magnetic moments

accumulation on Fermi surfaces of the KWS. The net magnetic moments on Fermi surfaces basically have two origins: (1) the SOC induced spin splitting; (2) the finite orbital magnetic moment distribution on Fermi surfaces. The twofold Kramers Weyl point we focused on in this work contributes to both the spin and orbital magnetic moments, but for a general KWS of chiral crystal symmetry, the complicated band structure diversifies the origin of magnetic moments on Fermi surfaces.

As we have seen, the Fermi pockets enclosing multi-fold fermion contribute to the magnetoelectric susceptibility as well. It is due to the fact that multi-fold fermion endows orbital magnetic moments to the Fermi surfaces outside. Along with the SOC induced spin splitting, the Fermi pockets enclosing multi-fold fermion can also give rise to spin and orbital magnetization driven by charge current⁴⁶. In a KWS, the magnetoelectric response from the multi-fold fermion and twofold Kramers Weyl point is the same type as the response tensor form is determined by the chiral crystal symmetry of the KWS. Since the Fermi surfaces with a multi-fold fermion inside have different magnetic moment, group velocity and density of states from that with a twofold Kramers Weyl point, the magnetoelectric susceptibility can differ in the value for the two cases.

Besides the twofold Kramers Weyl point and multi-fold fermion at high symmetry points in the Brillouin zone, a Weyl point at a general \mathbf{k} point can generate finite longitudinal magnetoelectric susceptibility as long as the crystal symmetry does not reduce it to zero. This is the case of the local maximal magnetoelectric susceptibility α_0 of RhSn at $E = -0.46$ eV shown in Fig. 3b. There is a Weyl point in $\Gamma - R$ line around the energy of $E = -0.46$ eV which enhances the magnetoelectric susceptibility at that energy. In a brief summary, the longitudinal magnetoelectric susceptibility in KWS of chiral crystal symmetry originates from SOC and Weyl points in the band structure. The magnitude of longitudinal magnetoelectric response at given current density relies on the Fermi surface magnetic moment, Fermi velocity, effective scattering time and density of states at the Fermi energy of KWS.

Concerning the applications of KWS, due to its unique longitudinal magnetoelectric response, the KWS/ferromagnet heterostructures can be used for new designs of spin-orbit torque devices as shown in Fig. 4a. It is interesting to note that a KWS can cause current induced magnetization switching in the ferromagnetic layer by two effects. First, as depicted in Fig. 4a, the KWS can inject electrons which carry both orbital and spin angular momentum into the ferromagnetic layer. The injection of angular momentum can cause magnetization switching similar to the spin transfer torque induced magnetization switching in magnetic tunneling junctions as shown in Fig. 4b. The important

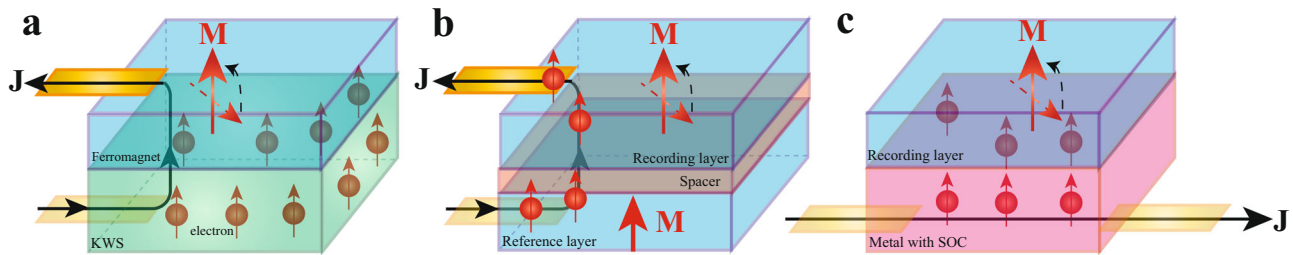


Fig. 4 The schematics of current induced magnetization switching in spintronic devices. **a** A Kramer's Weyl semimetal/ferromagnet heterostructure. When a current \mathbf{J} passes through the Kramer's Weyl semimetal, the effective magnetic field at the Kramer's Weyl semimetal and the electrons injected from Kramer's Weyl semimetal to the ferromagnetic layer provide a torque to switch the magnetization direction (\mathbf{M}) of the ferromagnetic layer. **b** A magnetic tunneling junction. The junction is made of a reference ferromagnetic layer and the recording ferromagnetic layer separated by a metallic or insulating spacer. The magnetization of the recording layer can be switched by the spin polarized electrons coming out of the reference layer. **c** A spin-orbit torque device^{30–33}. The current induces magnetization at the metal layer through magnetoelectric effect (or the inverse spin galvanic effect). The effective magnetic field at the metal/ferromagnet interface causes the magnetization switching in the ferromagnetic layer.

difference is that the electrons injected by KWS can carry both orbital and spin angular momentum. Particularly, close to the Weyl points, the orbital magnetization carried by the electrons can be significant. Therefore, KWS can work as a source of spin and orbital angular momentum for magnetization switching. Second, when a current is passed along the principal symmetry axis of the KWS, a magnetization is induced at interface between the KWS and the ferromagnet. This current induced magnetization can cause the magnetization switching of the ferromagnet layer through ferromagnetic coupling between the KWS and the ferromagnet.

In recent years, tremendous progress has been made for the study of spin-orbit torque devices as depicted in Fig. 4c. For example, current induced magnetization switching due to spin-orbit torques, in the presence of an in-plane magnetic field, has been realized experimentally in heavy metal/ferromagnet heterostructures^{49,50}. It was also demonstrated that charge currents in multi-layer WTe_2 can induce out-of-plane magnetizations³² and WTe_2 can also be used for magnetization switching for ferromagnets with in-plane anisotropy⁵¹. However, an all electric control of magnetization switching for ferromagnets with perpendicular magnetic anisotropy (PMA) through spin-orbit torques, which is important for high density magnetic memories, has not been experimentally realized. Therefore, due to the unique longitudinal response of KWS, they allow new designs of spintronic devices for magnetization switching of ferromagnets with perpendicular magnetic anisotropy as depicted in Fig. 4a.

Concerning the candidate materials of KWS, the cubic chiral B20 structured materials³⁴, such as the recent experimentally studied RhSi ¹⁹, CoSi ^{19–21}, AlPt ²², PtGa ²³, PdGa ²⁴, and RhGe , RhSn all belong to the T point group that has the isotropic longitudinal magnetoelectric response. Particularly, the PtGa ²³ that has the strongest SOC reported so far in chiral crystals is expected to produce strong longitudinal magnetoelectric effect. Besides, elemental Se and Te also have chiral lattice structure^{35,36}. Interestingly, a few superconducting materials with chiral lattice symmetry and strong spin-orbit coupling such as $\text{Li}_2\text{Pt}_3\text{B}$ ⁵², $\text{Li}_2\text{Pd}_3\text{B}$ ⁵³, $\text{Mo}_3\text{Al}_2\text{C}_5$ ⁵⁴, TaRh_2B_2 and NbRh_2B_2 ⁵⁵ have been experimentally studied. In their normal state, these superconducting materials can also have spintronic applications.

In conclusion, the magnetoelectric effect of KWS are studied in this work using three different methods: 1. Group theory analysis; 2. Analytical calculations through linear response theory; and 3. Realistic tight-binding calculations are constructed through first principle calculations and the magnetoelectric response of realistic materials are calculated. A new design for current-controlled magnet memory device is proposed and new candidates of KWS are suggested.

Methods

Symmetry analysis for the magnetoelectric response in Chiral crystals. In the chiral crystals with magnetoelectric effect $M_i = \sum_j \alpha_{ij} E_j$ with $i, j = x, y, z$, under the crystal symmetry the magnetization transforms as $M_i \rightarrow \det(\hat{R}) \hat{R}_{ij} M_j$ while the electric field transforms as $E_i \rightarrow \hat{R}_{ij} E_j$, where \hat{R} represents the symmetry transformation operator and is an orthogonal matrix. As a result, the magnetoelectric susceptibility α_{ij} under the crystal symmetry respects

$$\alpha = \det(\hat{R}) \hat{R} \alpha \hat{R}^T. \quad (9)$$

The chiral point groups, which do not allow improper rotations, can be divided into three sub-classes: the cubic point groups $\{T, O\}$, the dihedral point groups $\{D_n\}$ with $n = 2, 3, 4, 6$ and the cyclic point groups C_n with $n = 1, 2, 3, 4, 6$. In the cubic point groups $\{T, O\}$, the multiple high order rotation axes along different directions would force the magnetoelectric susceptibility to be proportional to the identity matrix. In the dihedral point groups $\{D_n\}$ with $n = 2, 3, 4, 6$, the C_n rotation axis along z and the in-plane C_2 rotation axis along the x -axis would eliminate all the off diagonal elements and leave only the diagonal elements in the magnetoelectric susceptibility $\alpha = \text{diag}\{\alpha_{xx}, \alpha_{yy}, \alpha_{zz}\}$. In $\{D_3, D_4, D_6\}$, the principal axis would further make $\alpha_{xx} = \alpha_{yy}$. In the cyclic point groups $\{C_n\}$ with $n = 1, 2, 3, 4, 6$, the lower symmetry would allow the off-diagonal elements to coexist with the diagonal elements. The explicit forms of the magnetoelectric susceptibility pseudotensor α_{ij} from the symmetry analysis is shown in Table 1 for the 11 chiral point groups.

Magnetoelectric susceptibility in isotropic KWS. In the isotropic KWS, at the Fermi energy $E_F = \frac{\hbar^2 k^2}{2m} \pm \hbar v |k|$, there are two spherical Fermi surfaces with the corresponding wave vectors $\mathbf{k}_{F\pm} = k_{F\pm} \hat{\mathbf{k}}$ and $k_{F\pm} = \frac{1}{\hbar} (\sqrt{2mE_F + m^2 v^2} \mp mv)$, $\hat{\mathbf{k}} = \frac{\mathbf{k}}{|\mathbf{k}|}$. On the Fermi surfaces enclosing the Kramer's Weyl point, the spin magnetic dipole moment and orbital magnetic dipole moment are respectively

$$\mathbf{S}_{\mathbf{k}_{F\pm}} = \pm \frac{g \hbar}{2} \frac{e \hbar}{2m_e} \hat{\mathbf{k}}_{F\pm}, \quad \mathbf{m}_{\mathbf{k}_{F\pm}} = \pm \frac{1}{2} \frac{e v}{|\mathbf{k}_{F\pm}|} \hat{\mathbf{k}}_{F\pm}, \quad (10)$$

with \pm denoting the two band branches. The density of states can be obtained as

$$N_{\pm}(E_F) = \frac{m}{2\pi^2 \hbar^3} \left(\sqrt{2mE_F + m^2 v^2} + \frac{mv^2}{\sqrt{\frac{2E_F}{m} + v^2}} \mp 2mv \right), \quad (11)$$

and the Fermi velocities there become

$$\mathbf{v}_{\mathbf{k}_{F\pm}} = \sqrt{\frac{2E_F}{m} + v^2} \hat{\mathbf{k}}_{F\pm}. \quad (12)$$

At the Fermi energy, the magnetoelectric susceptibility α_0 can be approximated through $\sum_n \frac{1}{(2\pi)^3} \int_{\text{BZ}} \dots \frac{d^3(E_{n,\mathbf{k}})}{dE_{n,\mathbf{k}}} d\mathbf{k} \rightarrow -\sum_n N_n(E_F) \int \frac{d\Omega_{\mathbf{k}_{F\pm}}}{4\pi}$ with $n = \pm$ and then we can obtain

$$\alpha_0 = -\frac{e^2 v \tau}{6\hbar^2 \pi^2} \sqrt{2mE_F + m^2 v^2} \left(g \frac{m}{m_e} - 1 \right). \quad (13)$$

Isotropic Weyl SOC suppressed back scattering. In the pure scalar potential scattering process

$$\mathcal{H}_{\text{imp}} = \int d\mathbf{k} d\mathbf{k}' \psi_{\mathbf{k}}^\dagger V_{\mathbf{k}-\mathbf{k}'} \psi_{\mathbf{k}'}, \quad (14)$$

the scattering potential can be projected onto the band basis as

$$\hat{V}_{k-k'} = V_{k-k'} U_k^\dagger U_{k'}, \quad (15)$$

with

$$U_k = \begin{pmatrix} \cos \frac{\theta}{2} e^{-i\phi} & \sin \frac{\theta}{2} e^{-i\phi} \\ \sin \frac{\theta}{2} & -\cos \frac{\theta}{2} \end{pmatrix}, \quad (16)$$

and θ, ϕ are the azimuth and polar angle of \mathbf{k} . In the presence of large SOC, the scattering is dominated in each band branch (\pm) and the effective scattering potential becomes

$$\hat{V}_{k-k',+} = V_{k-k'} \left[\cos \frac{\theta'}{2} \cos \frac{\theta}{2} e^{-i(\phi'-\phi)} + \sin \frac{\theta'}{2} \sin \frac{\theta}{2} \right] \quad (17)$$

$$\hat{V}_{k-k',-} = V_{k-k'} \left[\sin \frac{\theta'}{2} \sin \frac{\theta}{2} e^{i(\phi'-\phi)} + \cos \frac{\theta'}{2} \cos \frac{\theta}{2} \right]. \quad (18)$$

In the Born approximation, the scattering in each band branch is obtained as

$$\frac{1}{\tau_{\pm}} = \frac{mk_{F\pm} n_{\text{imp}}}{4\pi^2 \hbar^3} \int_0^\pi d\vartheta \int_0^{2\pi} d\varphi \hat{V}_{k-k',\pm}^2 (1 - \cos \vartheta) \sin \vartheta, \quad (19)$$

with $\varphi = \phi' - \phi$, $\vartheta = \theta' - \theta$. In the spherical Fermi surfaces, the scattering potential $\hat{V}_{k-k',\pm}^2$ only depends on the angle between \mathbf{k} and \mathbf{k}' , so

$$\int_0^\pi d\vartheta \int_0^{2\pi} d\varphi \hat{V}_{k-k',\pm}^2 (1 - \cos \vartheta) \sin \vartheta = \frac{172}{105} k_{F\pm}^2, \quad (20)$$

$$\int_0^\pi d\vartheta \int_0^{2\pi} d\varphi V_{k-k',\pm}^2 (1 - \cos \vartheta) \sin \vartheta = \frac{16}{3} k_{F\pm}^2. \quad (21)$$

As a result, the Weyl SOC reduces the scattering potential to about 0.3 and suppresses the back scattering.

First-principles calculation and Wannier function construction. We perform first-principles calculation within the density functional theory framework as implemented in Vienna Abinitio Simulation Package (VASP)⁵⁶. PAW^{57,58} type of pseudopotential with PBE exchange functional⁵⁹ is used in the calculations and spin orbit coupling is included in the pseudopotentials. After the first-principle calculation is done, tight binding Hamiltonian which perfectly recovers bands near Fermi surface is built through Wannier function construction using package Wannier90^{60,61}. The lattice structures of all the materials we considered are obtained from the ICSD⁶².

Data availability

The data generated from our codes that support the findings of this study are available from the corresponding author upon reasonable request.

Received: 22 November 2020; Accepted: 23 February 2021;

Published online: 31 March 2021

References

- Wan, X., Vishwanath, A. & Savarasov, S. Y. Topological semimetal and Fermi-arc surface states in the electronic structure of pyrochlore iridates, *Phys. Rev. B* **83**, (2011).
- Balents, L. Weyl electrons kiss. *Physics* **4**, 36 (2011).
- Burkov, A. A. & Balents, L. Weyl semimetal in a topological insulator multilayer. *Phys. Rev. Lett.* **107**, 127205 (2011).
- Weng, H., Fang, C., Fang, Z., Bernevig, B. A. & Dai, X. Weyl semimetal phase in noncentrosymmetric transition-metal monophosphides. *Phys. Rev. X* **5**, 011029 (2015).
- Nielsen, H. B. & Ninomiya, M. The Adler-Bell-Jackiw anomaly and Weyl fermions in a crystal. *Phys. Lett. B* **130**, 389 (1983).
- Son, D. T. & Yamamoto, N. Berry curvature, triangle anomalies, and the chiral magnetic effect in fermi liquids. *Phys. Rev. Lett.* **109**, 181602 (2012).
- Huang, X. et al. Observation of the chiral-anomaly-induced negative magnetoresistance in 3D Weyl semimetal TaAs. *Phys. Rev. X* **5**, 031023 (2015).
- Zhang, C.-L. et al. Signatures of the Adler-Bell-Jackiw chiral anomaly in a Weyl fermion semimetal. *Nat. Commun.* **7**, 10735 (2016).
- Xu, S.-Y. et al. Discovery of a Weyl fermion semimetal and topological Fermi arcs. *Science* **347**, 294 (2015).
- Lv, B. Q. et al. Experimental discovery of Weyl semimetal TaAs. *Phys. Rev. X* **5**, 031013 (2015).
- Potter, A. C., Kimchi, I. & Vishwanath, A. Quantum oscillations from surface Fermi arcs in Weyl and Dirac semimetals. *Nat. Commun.* **5**, 5161 (2014).
- Chan, C.-K., Lee, P.-A., Burch, K. S., Han, J. H. & Ran, Y. When chiral photons meet chiral fermions: photoinduced anomalous Hall effects in Weyl semimetals. *Phys. Rev. Lett.* **116**, 026805 (2016).
- Chan, C.-K., Linder, N. H., Refael, G. & Lee, P.-A. Photocurrents in Weyl semimetals. *Phys. Rev. B* **95**, 041104(R) (2017).
- Juan, F., Grushin, A. G., Morimoto, T. & Moore, J. E. Quantized circular photogalvanic effect in Weyl semimetals. *Nat. Commun.* **8**, 15995 (2017).
- Bradlyn, B. et al. Beyond Dirac and Weyl fermions: unconventional quasiparticles in conventional crystals. *Science* **353**, 6299 (2016).
- Tang, P., Zhou, Q. & Zhang, S. C. Multiple types of topological fermions in transition metal silicides. *Phys. Rev. Lett.* **119**, 206402 (2017).
- Chang, G. et al. Unconventional chiral fermions and large topological Fermi arcs. *Phys. Rev. Lett.* **119**, 206401 (2017).
- Chang, G. et al. Topological quantum properties of chiral crystals. *Nat. Mater.* **17**, 978–985 (2018).
- Sanchez, D. S. et al. Topological chiral crystals with helicoid-arc quantum states. *Nature* **567**, 500–505 (2019).
- Rao, Z. et al. Observation of unconventional chiral fermions with long Fermi arcs in CoSi. *Nature* **567**, 496–499 (2019).
- Takane, D. et al. Observation of chiral fermions with a large topological charge and associated Fermi-arc surface states in CoSi. *Phys. Rev. Lett.* **122**, 076402 (2019).
- Schroter, N. B. M. et al. Chiral topological semimetal with multifold band crossings and long Fermi arcs. *Nat. Phys.* **15**, 759 (2019).
- Yao, M. et al. Observation of giant spin-split Fermi-arc with maximal Chern number in the chiral topological semimetal PtGa. *Nat. Commun.* **11**, 2033 (2020).
- Schroter, N. B. M. et al. Observation and control of maximal Chern numbers in a chiral topological semimetal. *Science* **369**, 179 (2020).
- Edelstein, V. M. Spin polarization of conduction electrons induced by electric current in two-dimensional asymmetric electron systems. *Solid State Commun.* **73**, 233 (1990).
- Zhong, S., Moore, J. E. & Souza, I. Gyrotropic magnetic effect and the magnetic moment on the Fermi surface. *Phys. Rev. Lett.* **116**, 077201 (2016).
- Ma, J. & Pesin, D. A. Chiral magnetic effect and natural optical activity in metals with or without Weyl points. *Phys. Rev. B* **92**, 235205 (2015).
- Johansson, A., Henk, J. & Mertig, I. Theoretical aspects of the Edelstein effect for anisotropic two-dimensional electron gas and topological insulators. *Phys. Rev. B* **93**, 195440 (2016).
- Johansson, A., Henk, J. & Mertig, I. Edelstein effect in Weyl semimetals. *Phys. Rev. B* **97**, 085417 (2018).
- Manchon, A. et al. Current-induced spin-orbit torques in ferromagnetic and antiferromagnetic systems. *Rev. Mod. Phys.* **91**, 035004 (2019).
- Sinova, J. & Jungwirth, T. Surprises from the spin Hall effect. *Phys. Today* **70**, 38 (2017).
- MacNeill, D. et al. Control of spin-orbit torques through crystal symmetry in WTe₂/ferromagnet bilayers. *Nat. Phys.* **13**, 300–305 (2017).
- Ciccarelli, C. et al. Room-temperature spin-orbit torque in NiMnSb. *Nat. Phys.* **12**, 855–860 (2016).
- Severin, D. A. P. & Burkov, A. T. Electronic Structure of B20 (FeSi-Type) Transition Metal Monosilicides. *Materials* **12**, 2710 (2019).
- Hirayama, M., Okugawa, R., Ishibashi, S., Murakami, S. & Miyake, T. Weyl node and spin texture in trigonal tellurium and selenium. *Phys. Rev. Lett.* **114**, 206401 (2015).
- Furukawa, T., Shimokawa, Y., Kobayashi, K. & Itou, T. Observation of current induced bulk magnetization in elemental tellurium. *Nat. Commun.* **8**, 954 (2017).
- Sakano, M. Radial Spin Texture in Elemental Tellurium with Chiral Crystal Structure. *Phys. Rev. Lett.* **124**, 136404 (2020).
- Furukawa, T., Watanabe, Y., Ogasawara, N., Kobayashi, K. & Itou, T. Chirality-Induced Electrical Generation of Magnetism in Nonmagnetic Elemental Tellurium. *arXiv:2010.09210*.
- Xiao, D., Chang, M.-C. & Niu, Q. Berry phase effects on electronic properties. *Rev. Mod. Phys.* **82**, 1959 (2010).
- He, W.-Y. & Law, K. T. Magnetolectric effects in gyrotropic superconductors. *Phys. Rev. Res.* **2**, 012073(R).
- Roushan, P. et al. Topological surface states protected from backscattering by chiral spin texture. *Nature* **60**, 1106–1109 (2009).
- Zhang, T. et al. Experimental demonstration of topological surface states protected by time-reversal symmetry. *Phys. Rev. Lett.* **103**, 266803 (2009).
- Lee, W.-C., Wu, C., Arovas, D. P. & Zhang, S.-C. Quasiparticle interference on the surface of the topological insulator Bi₂Te₃. *Phys. Rev. B* **80**, 245439 (2009).
- Ramshaw, B.-J. et al. Quantum limit of transport and destruction of the Weyl nodes in TaAs. *Nat. Commun.* **9**, 2217 (2018).
- Zhang, C.-L. et al. Electron scattering in tantalum monoarsenide. *Phys. Rev. B* **95**, 085202 (2017).
- Flicker, F. et al. Chiral optical response of multifold fermions. *Phys. Rev. B* **98**, 155145 (2018).

47. Yoda, T., Yokoyama, T. & Murakami, S. Current-induced orbital and spin magnetizations in crystals with helical structure. *Sci. Rep.* **5**, 12024 (2015).
48. Yoda, T., Yokoyama, T. & Murakami, S. Orbital Edelstein effect as a condensed-matter analog of solenoid. *Nano. Lett.* **18**, 916–920 (2018).
49. Miron, I. M. et al. Perpendicular switching of a single ferromagnetic layer induced by in-plane current injection. *Nature* **476**, 189–193 (2011).
50. Li, P. et al. Spin-orbit torque-assisted switching in magnetic insulator thin films with perpendicular magnetic anisotropy. *Nat. Commun.* **7**, 12688 (2016).
51. Li, S. et al. All-electric magnetization switching and Dzyaloshinskii-Moriya interaction in WTe₂/ferromagnet heterostructures. *Nat. Nanotech.* **14**, 945–949 (2019).
52. Yuan, H. Q. S-wave spin-triplet order in superconductors without inversion symmetry: Li₂Pd₃B and Li₂Pt₃B. *Phys. Rev. Lett.* **97**, 017006 (2006).
53. Togano, K. et al. Superconductivity in the metal rich Li-Pd-B ternary boride. *Phys. Rev. Lett.* **93**, 247004 (2004).
54. Karki, A. B. et al. Structure and physical properties of the noncentrosymmetric superconductor Mo₃Al₂C. *Phys. Rev. B* **82**, 064512 (2010).
55. Carnicom, E. M. et al. TaRh₂B₂ and NbRh₂B₂: Superconductors with a chiral noncentrosymmetric crystal structure. *Sci. Adv.* **4**, 7969 (2018).
56. Kresse, G. & Furthmüller, J. Efficiency of ab-initio total energy calculations for metals and semiconductors using a plane-wave basis set. *Comput. Mater. Sci.* **6**, 15–50 (1996).
57. Blochl, P. E. Projector augmented-wave method. *Phys. Rev. B* **50**, 17953 (1994).
58. Kresse, G. & Joubert, D. From ultrasoft pseudopotentials to the projector augmented-wave method. *Phys. Rev. B* **59**, 1798 (1999).
59. Perdew, J. P., Burke, K. & Ernzerhof, M. Generalized gradient approximation made simple. *Phys. Rev. Lett.* **77**, 3865 (1996).
60. Souza, I., Marzari, N. & Vanderbilt, D. Maximally localized Wannier functions for entangled energy bands. *Phys. Rev. B* **65**, 035109 (2001).
61. Mostofi, A. A. et al. Wannier90: A tool for obtaining maximally-localised Wannier functions. *Comput. Phys. Commun.* **178**, 685–699 (2008).
62. Inorganic Crystal Structure Database (FIZ Karlsruhe, 2014); <http://icsd.fiz-karlsruhe.de/icsd>

Acknowledgements

We thank Xi Dai, Kin Fai Mak, Qiming Shao and Binghai Yan for inspiring discussions. K.T.L. is thankful for the support of HKRGC through C6026-16W, 16324216, 16307117

and 16309718. K.T.L. is further supported by the Croucher Foundation and the Dr. Tai-chin Lo Foundation.

Author contributions

K.T.L. and W.-Y.H. conceived the idea and initiated the project. W.-Y.H. performed the symmetry analysis and the theoretical calculation of the magnetoelectric susceptibility. X. Y.X. performed the first principles calculation and Wannier function construction for the selected Kramers Weyl semimetals in this work. All the authors discussed the results and co-wrote the paper.

Competing interests

The authors declare no competing interests.

Additional information

Supplementary information The online version contains supplementary material available at <https://doi.org/10.1038/s42005-021-00564-w>.

Correspondence and requests for materials should be addressed to W.-Y.H. or K.T.L.

Reprints and permission information is available at <http://www.nature.com/reprints>

Publisher's note Springer Nature remains neutral with regard to jurisdictional claims in published maps and institutional affiliations.



Open Access This article is licensed under a Creative Commons Attribution 4.0 International License, which permits use, sharing, adaptation, distribution and reproduction in any medium or format, as long as you give appropriate credit to the original author(s) and the source, provide a link to the Creative Commons license, and indicate if changes were made. The images or other third party material in this article are included in the article's Creative Commons license, unless indicated otherwise in a credit line to the material. If material is not included in the article's Creative Commons license and your intended use is not permitted by statutory regulation or exceeds the permitted use, you will need to obtain permission directly from the copyright holder. To view a copy of this license, visit <http://creativecommons.org/licenses/by/4.0/>.

© The Author(s) 2021